RESEARCH ARTICLE SUMMARY

IMMUNOLOGY

Primordial GATA6 macrophages function as extravascular platelets in sterile injury

J. Zindel, M. Peiseler, M. Hossain, C. Deppermann, W. Y. Lee, B. Haenni, B. Zuber, J. F. Deniset, B. G. J. Surewaard, D. Candinas, P. Kubes*

INTRODUCTION: Most multicellular organisms have a major body cavity that harbors immune cells. In primordial species such as the purple sea urchin, these cells—called coelomocytes—fulfill dual functions. Sea urchin coelomocytes clear pathogens from the peritoneal compartment, but they have also been shown to form multicellular aggregates that adhere to injured tissue and are crucial for repair. In mammals, the peritoneal, pleural, and pericardial cavities are filled with vast numbers of resident GATA6$^+$ cavity macrophages. The role of peritoneal cavity macrophages as phagocytes in clearing pathogens has been established for decades. Recent evidence suggests that these cells migrate to injuries within the peritoneal cavity, where they have been shown to promote tissue repair.

RATIONALE: It remains unclear how cavity macrophages, which are suspended in the fluid phase (peritoneal fluid), can identify injuries, which can be several thousand micrometers away, and how they can exhibit chemotaxis over that distance through a fluid-filled compartment that is under constant convective flow. In this study, we developed an intravital microscopy (IVM) model to study the dynamics and molecular mechanisms of resident GATA6$^+$ macrophage recruitment in the peritoneal cavity after injury.

RESULTS: By using inverted multiphoton IVM with extremely sensitive non-descanned hybrid detectors, we were able to image the peritoneal cavity through the intact abdominal wall in living animals. The tracks of the rapidly moving peritoneal macrophages showed that they passively traversed the peritoneal cavity in a respiration-dependent and seemingly random pattern. Next, we used a focused high-power infrared laser beam to induce focal injuries to the peritoneum, and we imaged the subsequent immune response. We found that peritoneal macrophages were rapidly recruited through a two-step process: (i) an initial tether of macrophages to the injury site, followed by (ii) secondary tethers that formed an aggregate reminiscent of a thrombus-like structure in response to injury. Macrophage aggregation mirrored and rivaled the speed of platelet aggregation (thrombus formation) in the adjacent vasculature. By probing the transcriptome of peritoneal macrophages and a targeted series of knockout and inhibition IVM experiments, we found that peritoneal macrophage aggregation was independent of canonical mammalian adhesion molecules such as integrins, selectins, and immunoglobulin-like adhesion molecules. Instead, peritoneal macrophage aggregation was dependent on primordial scavenger receptor cysteine-rich (SRCR) domains. SRCR domains are highly conserved among species, with many homologs expressed by sea urchin coelomocytes and sea sponges, and some of these proteins have been identified as cell-cell adhesion molecules in these primordial organisms. Aggregates of cavity macrophages physically sealed injuries and promoted rapid repair of focal peritoneal lesions. However, in abdominal surgery models that reflect iatrogenic surgical situations in which the peritoneal cavity is opened and foreign suture material is introduced, these cavity macrophages formed extensive aggregates that promoted the growth of intra-abdominal scar tissue called peritoneal adhesions. These peritoneal adhesions cause substantial morbidity for patients and considerable costs for health care systems. We showed that the number and tenacity of peritoneal adhesions was significantly reduced by either depleting peritoneal macrophages or therapeutically inhibiting their scavenger receptor–dependent recruitment and aggregation.

CONCLUSION: Our results unveil a platelet-like extravascular fluid-phase response by macrophages. This rapid response seals the peritoneal leaks within minutes and serves an important function in repairing small injuries such as focal thermal or laser-induced peritoneal injuries. We hypothesize that such focal injuries reflect a type of injury for which the immune system has evolved a beneficial response. By contrast, iatrogenic procedures, such as abdominal surgery involving implantation of foreign material, reflect a type of injury that has no evolutionary precedent. In this scenario, peritoneal macrophages may cause detrimental scarring, instead of restitution ad integrum, in an attempt to repair the wound. Thus, macrophage aggregation and its inhibition by scavenger receptor antagonists are of clinical importance and may provide a therapeutic target to prevent scar formation after surgery in the peritoneal cavity. Furthermore, these findings may extend to other cavities, including pleural and pericardial spaces. ■

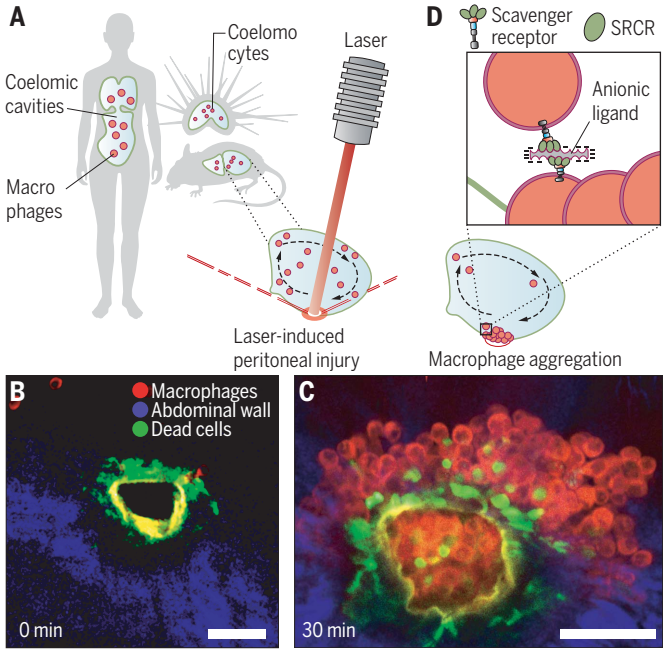

Aggregation of GATA6$^+$ peritoneal cavity macrophages in response to laser-induced peritoneal injury. (**A**) Human, mouse, and sea urchin coelomic cavities (mouse example enlarged) with circulating coelomocytes and macrophages. Injuries were induced by a multiphoton laser. (**B**) IVM image immediately after injury. Scale bar, 50 μm. (**C**) IVM image 30 min after injury. Scale bar, 50 μm. (**D**) Aggregation was dependent on scavenger receptors and a (yet unknown) polyanionic ligand.

The list of author affiliations is available in the full article online
*Corresponding author. Email: pkubes@ucalgary.ca
Cite this article as J. Zindel *et al.*, *Science* **371**, eabe0595 (2021). DOI: 10.1126/science.abe0595

READ THE FULL ARTICLE AT
https://doi.org/10.1126/science.abe0595

RESEARCH ARTICLE

IMMUNOLOGY

Primordial GATA6 macrophages function as extravascular platelets in sterile injury

J. Zindel[1,2,3,4], M. Peiseler[1,2,3], M. Hossain[1,2,3], C. Deppermann[1,2,3,5], W. Y. Lee[1,2], B. Haenni[6], B. Zuber[6], J. F. Deniset[1,2,3,7,8], B. G. J. Surewaard[1,2,3], D. Candinas[4], P. Kubes[1,2,3]*

Most multicellular organisms have a major body cavity that harbors immune cells. In primordial species such as purple sea urchins, these cells perform phagocytic functions but are also crucial in repairing injuries. In mammals, the peritoneal cavity contains large numbers of resident GATA6$^+$ macrophages, which may function similarly. However, it is unclear how cavity macrophages suspended in the fluid phase (peritoneal fluid) identify and migrate toward injuries. In this study, we used intravital microscopy to show that cavity macrophages in fluid rapidly form thrombus-like structures in response to injury by means of primordial scavenger receptor cysteine-rich domains. Aggregates of cavity macrophages physically sealed injuries and promoted rapid repair of focal lesions. In iatrogenic surgical situations, these cavity macrophages formed extensive aggregates that promoted the growth of intra-abdominal scar tissue known as peritoneal adhesions.

Most multicellular organisms have a major structure called the coelomic cavity, which compartmentalizes vital organs (*1*). In early metazoans, coelomic cavities harbor immune cells called coelomocytes (*2*). Coelomocytes in primitive species such as the purple sea urchin (*Strongylocentrotus purpuratus*) fulfill phagocyte functions for the clearance of toxins and pathogens (*3*–*6*) but are also crucial for tissue repair. In sea urchins, injuries to the coelomic cavity lead to the rapid aggregation of coelomocytes, a response that physically seals potential leaks and thus is crucial in preventing any breach (*7*). This reaction entails the calcium-dependent formation of stable coelomocyte cell-cell adhesions. This is functionally similar to what platelets do at an injury site in organisms with hematic circulatory systems, although details differ greatly on a molecular level (*8*). Thus, coelomocytes function as both platelets as well as phagocytes in echinoids, which lack the closed hematic circulatory system found in mammals.

[1]Department of Pharmacology and Physiology, University of Calgary, Calgary, Alberta, Canada. [2]Snyder Institute for Chronic Diseases, Cumming School of Medicine, University of Calgary, Calgary, Alberta, Canada. [3]Department of Microbiology, Immunology and Infectious Diseases, Cumming School of Medicine, University of Calgary, Calgary, Alberta, Canada. [4]Department of Visceral Surgery and Medicine, Department for BioMedical Research (DBMR), University of Bern, Bern, Switzerland. [5]Institute of Clinical Chemistry and Laboratory Medicine, University Medical Center Hamburg-Eppendorf, Hamburg, Germany. [6]Institute of Anatomy, University of Bern, Bern, Switzerland. [7]Department of Cardiac Sciences, Cumming School of Medicine, University of Calgary, Calgary, Alberta, Canada. [8]Libin Cardiovascular Institute of Alberta, University of Calgary, Calgary, Alberta, Canada.
*Corresponding author. Email: pkubes@ucalgary.ca

Mammals also have a coelomic body cavity, divided into three components: peritoneum, pleura, and pericardium. All of these cavities have a resident macrophage population characterized by expression of the transcription factor GATA6. These cavity macrophages are well recognized for their phagocytic functions (*9*, *10*) and have the capacity to form free-floating clots or aggregates to immobilize bacteria (*11*). We recently described the ability of cavity macrophages to locate and repair injury within body cavities (*12*). However, the mechanism by which these cavity cells suspended in the fluid phase (peritoneal fluid) identify injuries and rapidly follow chemotactic stimuli, presumably established in fluid, to migrate to a site of injury was unclear. Here we show that cavity macrophages are extravascular counterparts to platelets, forming rapid thrombus-like structures in response to injury that mirror and rival the speed of platelet thrombus formation in the adjacent vasculature. We show that cavity macrophage aggregation depends on primordial scavenger receptor domains, with many homologs expressed by sea urchin coelomocytes. Aggregates of cavity macrophages physically seal injuries and promote repair of focal lesions. However, with more complex injuries, cavity macrophages form extensive aggregates that promote the growth of intra-abdominal scar tissue called adhesions, which results in substantial morbidity.

Imaging of Gata6$^+$ cavity macrophages

To study the migration of Gata6$^+$ cavity macrophages in response to injury, we established a mouse intravital microscopy model. We found that any perturbation, including opening of the peritoneal cavity or introducing an imaging window, was sufficient to alter the biology of these cells. Within minutes of placing an imaging window into the cavity, GATA6$^+$ macrophages rapidly covered the foreign surface (fig. S1, A and B). To bypass this window artifact, we used multiphoton microscopy and extremely sensitive hybrid detectors to image the peritoneal cavity through the intact abdominal wall. The midline zone that separates the rectus abdominis muscles (the linea alba) provided a natural imaging window (Fig. 1, A and B; fig. S1, C and D; and movie S1). The abdominal wall was immobilized by the formation of an anchored pouch (Fig. 1, B and C). The pouch remained open to the remainder of the peritoneal cavity such that convection of peritoneal fluid was maintained, and organs could move within the space. Only the abdominal wall was immobilized. This model—referred to as the "open-pouch model" (Fig. 1D)—preserved the dynamics of peritoneal fluid motion (fig. S1E). Fast (8 kHz) resonant scanning enabled tracking of the rapidly moving peritoneal macrophages, which passively traversed the peritoneal cavity in a respiration-dependent and seemingly random pattern (fig. S1E) with speeds of up to 800 μm/s (fig. S1E). This observation accurately represented what we observed in the whole peritoneum. However, motion artifacts prevented continuous imaging outside the pouch.

These GATA6$^+$ macrophages were free-floating in the peritoneal fluid, were highly mobile, and differed from the GATA6$^-$ macrophages embedded in the muscular abdominal wall, a compartment that is well separated from the peritoneal cavity by the mesothelium. These abdominal wall macrophages are sessile and capable of cloaking a single dead cell (but not more) with their dendrites after laser injury to prevent neutrophil-driven inflammation (*13*). We studied the reaction of the free-floating GATA6$^+$ cavity macrophages to an injury of the peritoneal wall. Induction of a focal thermal injury by means of a multiphoton laser allowed us to precisely position the lesion so that it breached the mesothelial monolayer that compartmentalized the fluid-filled peritoneal cavity and also affected the most superficial layer of the muscular abdominal wall (fig. S1F). In the open-pouch model, the site of laser injury was covered with hundreds of cavity macrophages within minutes (Fig. 1, D and E; Movie 1; and movie S2). Notably, cavity macrophages seemed to form tight multicellular aggregates at the injury site. Use of a *Gata6*^{Venus} reporter mouse [instead of antibody against F4/80 (anti-F4/80)] demonstrated that this phenomenon was not caused by intraperitoneal fluid injection (fig. S1G), nor was the aggregation increased by agglutination through intraperitoneal application of the F4/80 staining antibody (fig. S1H). This

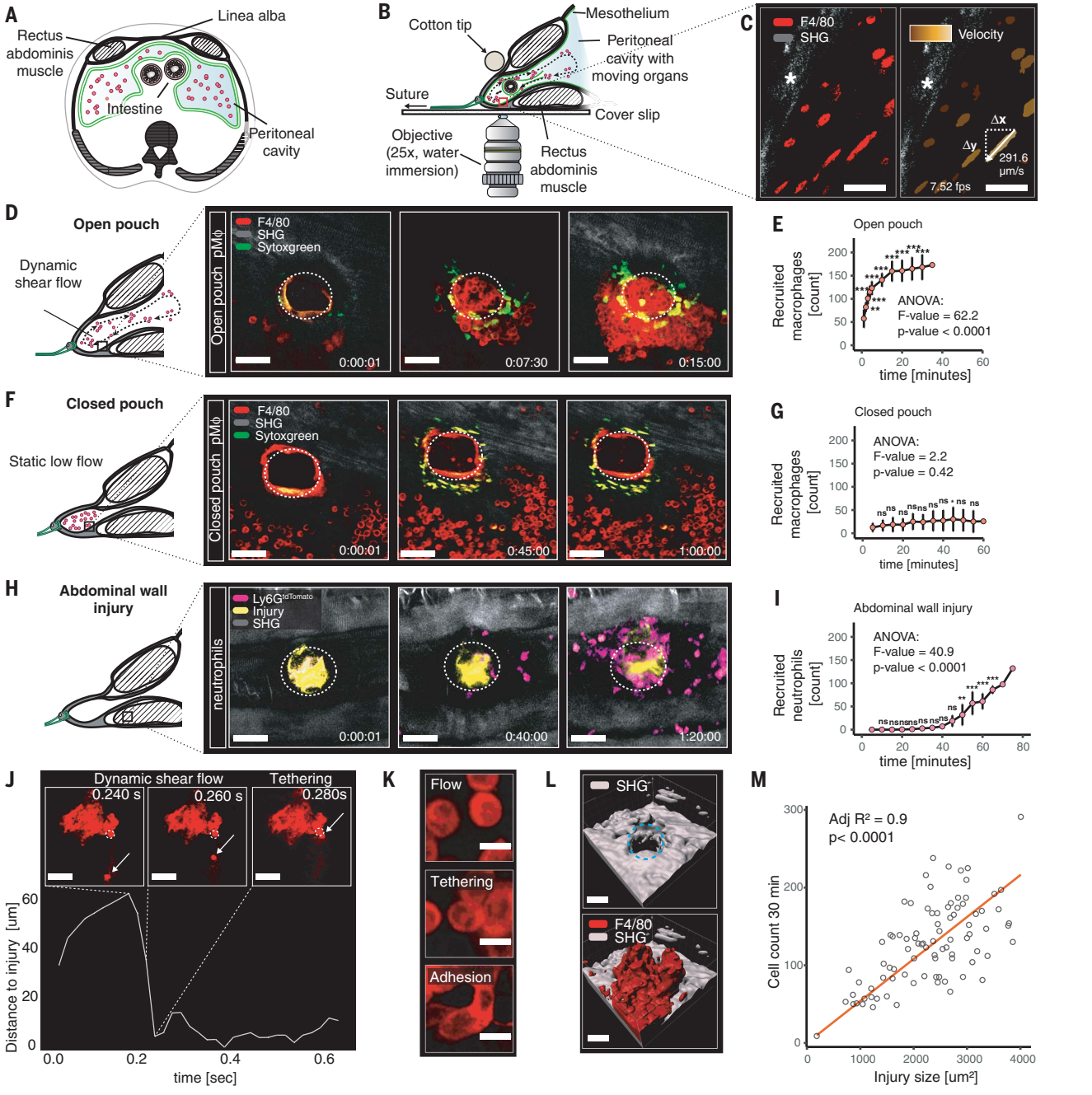

Fig. 1. Gata6^{+} cavity macrophages rely on passive transport for recruitment to laser-induced focal injury. (**A**) Anatomy of the peritoneal cavity. (**B**) Illustration of the abdominal-pouch IVM model. (**C**) Microscopic views of the pouch site show stable abdominal wall (asterisks) and mobile cavity macrophages (arrow). (**D**) Open-pouch IVM model with fluid movement. Dashed circles indicate transmesothelial laser injury. Cavity macrophages were stained with anti-F4/80 and dead cells with Sytox green (Movie 1). pMϕ, peritoneal macrophages. Scale bars, 50 µm. (**E**) Quantification of (D). (**F**) Closed-pouch IVM model with no fluid movement. Dashed circles indicate transmesothelial laser injury. Staining is same as in (D). Scale bars, 50 µm. (**G**) Quantification of (F). (**H**) Abdominal-pouch IVM preparation. Dashed circles indicate laser injury of the rectus abdominus muscle in the abdominal wall (dashed circle) of mice expressing *Ly6G*^{tdTomato} fluorescent neutrophil reporter. Scale bars, 50 µm. (**I**) Quantification of (H). (**J**) Resonant scanning mode with high frame rate (50 frames/s). Representative imaging (top) and tracking (bottom) are shown for one floating peritoneal macrophage (arrows) in relation to cells already aggregated (dashed circles). Scale bars, 50 µm. (**K**) Peritoneal cavity macrophages in different stages of aggregation. Scale bars, 10 µm. (**L**) Three-dimensional (3D) reconstruction of transmesothelial abdominal wall injury (dashed circle; top) and the resulting macrophage aggregation after 30 min (bottom). Scale bars, 50 µm. (**M**) Scatter plot and fitted linear regression line of cell count at injury versus injury size. Data are mean ± SD. n = 5, 4, and 3 replicates in (E), (G), and (I), respectively. P values were determined by repeated-measure one-way analysis of variance (ANOVA) (versus first time point): $^{*}P < 0.05$, $^{**}P < 0.01$, $^{***}P < 0.001$, not significant (ns) $P \geq 0.05$. Reported F values are for variability over time. P values and R^2 in (M) were determined by a linear regression model. Symbols in (M) represent individual observations (n = 89) from a total of n = 29 control (wild-type, untreated) animals of different experiments. All data are representative of $N \geq 3$ independent experiments. fps, frames per second; SHG, second harmonic generation (collagen).

Movie 1. Cavity macrophages form rapid aggregates to seal laser-induced peritoneal injury. Recruitment of F4/80+ cavity macrophages in response to laser-induced peritoneal injury is imaged by using the open-pouch IVM model. 3D reconstruction of the injured area after 30 min shows macrophage aggregates sealing the defect in the abdominal wall.

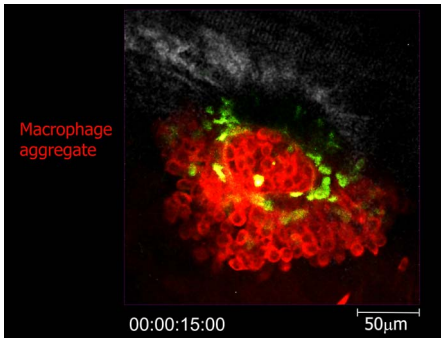

Movie 2. Intravital dynamics of macrophage and platelet aggregation. IVM is shown with head-to-head comparison of intravascular platelet aggregation and intraperitoneal macrophage aggregation in response to laser-induced injuries to the endothelium and mesothelium, respectively. Platelets were stained by intravenous application of anti-CD49b and macrophages by intraperitoneal administration of F4/80 antibody. Open-pouch IVM model images acquired 30 min after laser injury were three-dimensionally reconstructed. Injury size was increased to induce a peritoneal (mesothelial) injury as well as an endothelial injury in a nearby blood vessel. Macrophages were stained by intraperitoneal anti-F4/80 injection; platelets were stained by CD41-YFP fluorescent reporter.

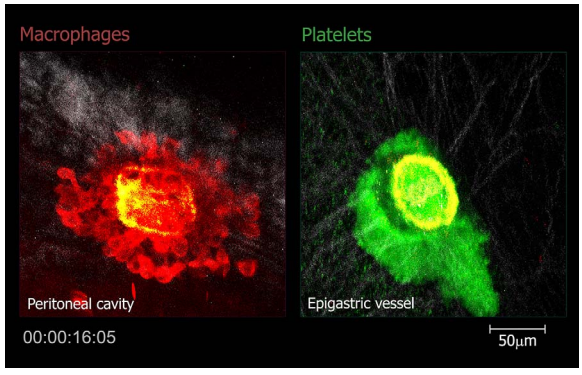

Movie 3. Uncontrolled cavity macrophage aggregation leads to adhesion formation. IVM with abdominal-window imaging shows uncontrolled macrophage aggregation 1 hour after window implantation, resulting in adhesion of intra-abdominal structures to macrophages aggregated on the window surface. Macrophages were stained with intraperitoneal anti-F4/80 injection.

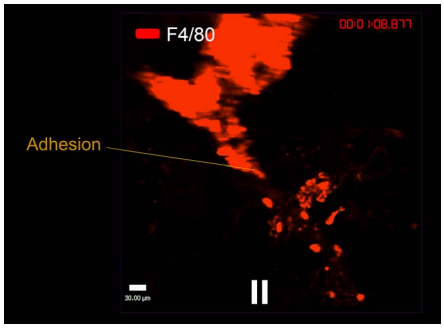

allowed for the subsequent use of F4/80 staining in various knockout mice.

Recruitment of Gata6$^+$ cavity macrophages

Because of the substantial similarity to platelet recruitment, we investigated whether macrophage recruitment required fluid shear flow. We constructed a peritoneal pouch and sealed it from the larger abdominal cavity (Fig. 1F), which eliminated the passive movement of cavity macrophages (fig. S1I). Despite the abundance of macrophages within the sealed pouch, lack of flow through the pouch abrogated the aggregate formation of GATA6$^+$ macrophages. In the closed-pouch model, significantly fewer cells were mobilized from suspension to the injury site, confirming that cavity macrophages rely on passive transportation by dynamic flow of the peritoneal fluid for their recruitment (Fig. 1, F and G; fig. S1J; and movie S3).

The cavity macrophage recruitment was notably different from the canonical recruitment of neutrophils, which exited blood vessels and crawled through the interstitial tissue in a directed manner to the site of injured abdominal wall (Fig. 1, H and I; fig. S1K; and movie S4). Moreover, the recruitment time was much slower for neutrophils (>40 min) than for cavity macrophages (1 to 15 min).

Using resonant scanning mode, we tracked cells in the fluid phase (fig. S2A). Macrophages in the fluid phase had a round appearance (Fig. 1, J and K). However, upon contact, the macrophages adopted an elongated epithelioid phenotype (Fig. 1K) and formed stable adhesions that were able to resist high fluid shear stress of up to 8 dyne/cm^2 (or 0.8 Pa) based on a velocity of 800 μm/s (fig. S1E) and an estimated viscosity of the peritoneal fluid approaching 1 Ps·s. Mean total peritoneal fluid volume of untreated mice was estimated to be 97 ± 15 μl (±SD) on the basis of the known concentration of urea (fig. S2B), yet no cells appeared to be resting on the mesothelium under basal conditions. Upon injury, a few macrophages tethered to the wounded area, with subsequent macrophages tethering directly to the already-attached macrophages (secondary tethers). Although some cells crawled, the net displacement was less than one to two cell lengths over the whole imaging period (fig. S2, C and D), which suggests that the initial tether, not chemotaxis, was the primary mode of localization to the injury site. At the injury, the cell-cell aggregates of cavity macrophages covered the induced breach of the mesothelium (Fig. 1L) but did not grow indefinitely, which suggests that a regulatory mechanism controlled aggregate size. There was a strong correlation between damage size and number of cells attached after 30 min (Fig. 1M). Thus, the recruitment of macrophages is a regulated two-step process: First, free-floating macrophages tether to the injury, and then additional macrophages form secondary tethers to these already-attached macrophages. No obvious chemotactic behavior could be seen at either step of this recruitment process.

Gata6$^+$ macrophages resemble extravascular platelets

The ability to rapidly form aggregates under shear at injury sites was reminiscent of platelet aggregation and thrombus formation after damage of the vessel wall. For comparison, we stained platelets with fluorescently labeled antibody against CD49b (anti-CD49b) and induced the same thermal laser injury to the epigastric vessel wall. A transendothelial injury elicited an intravascular platelet aggregation, which highly resembled cavity macrophage aggregation after transmesothelial injury (Fig. 2, A to C; Movie 2; and fig. S3, A and B). For a direct head-to-head comparison, *Itga2b*^{YFP} (CD41) reporter mice in which platelets constitutively express yellow fluorescent protein (YFP) were tracked together with intraperitoneal macrophages. Induction of a thermal injury spanning the vasculature (transendothelial) and peritoneal wall (transmesothelial) led to an intravascular platelet thrombus formation on one side of the injury and the formation of a macrophage aggregate on the other side (Fig. 2D and Movie 2). However, at no stage did the platelets and macrophages intermix, retaining localization in their respective compartments. Moreover, depletion of platelets did not affect the formation of the macrophage aggregate (fig. S3H), suggesting no cross-talk.

Nevertheless, the kinetics was markedly similar, and both platelet and macrophage aggregates reached a stable size after 15 min (Fig. 2C).

In echinoids, coelomocyte aggregation occurs spontaneously when macrophages are removed from the coelom (*7*, *8*). To probe the intrinsic aggregation capacity of peritoneal cavity macrophages, we used aggregometry, a method commonly used to assess platelet function in patients with bleeding disorders. Very much like coelomocytes, cavity macrophages formed spontaneous aggregates independent of serum or peritoneal fluid, a process that could be inhibited with EDTA (Fig. 2, E to H, and fig. S3, C to E). We were able to accelerate macrophage aggregation in vitro by using adenosine triphosphate (ATP), an established activator of platelet aggregation (Fig. 2, E to H). The time needed to reach maximal aggregation under shear was the same as the time needed for platelet aggregation (Fig. 2, E and G, and fig. S3, C to E). For comparison, we isolated blood neutrophils and subjected them to aggregometry. Under identical conditions to those used for macrophages, neutrophils showed no tendency to aggregate (fig. S3F). Furthermore, despite ample lymphocytes and mast cells within the peritoneal cavity, aggregates consisted only of macrophages when examined with electron microscopy (fig. S3G).

The molecular mechanism for macrophage aggregation

Next, we asked what controlled cavity macrophage adhesion and cluster formation at the injury site in vivo. Because the observed cell accumulation occurred within minutes, we hypothesized that the responsible adhesion molecules were constitutively expressed by cavity macrophages. We probed a transcriptomic profile of cavity macrophages, recently published by our group (*14*), for expression of canonical adhesion molecules such as integrins, selectins, and immunoglobulin (Ig)–like adhesion molecules. Cavity macrophages almost exclusively expressed integrin dimers that contained either the β1 or β2 chain but not prototypical platelet integrins such as α2bβ3 (fig. S4A). Combination of blocking antibodies against β1 (CD29) and β2 (CD18) integrins did not result in a reduction of adhering cells after 30 min (fig. S4B). Similarly, blocking PSGL (CD161), the ligand of both selectins expressed by cavity macrophages

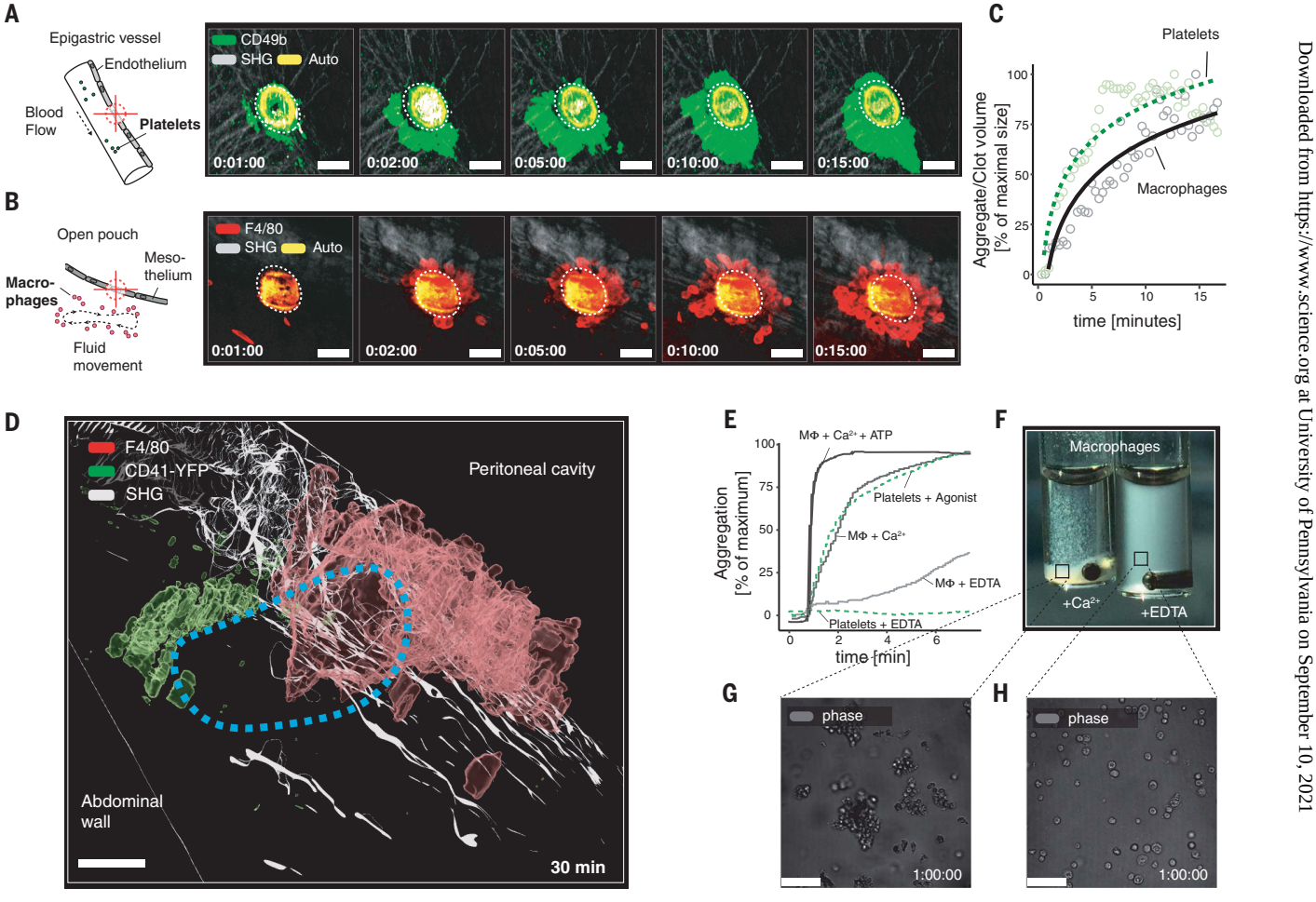

Fig. 2. Cavity macrophages as extravascular platelets. (**A**) IVM of epigastric blood vessels. Dashed circles denote transendothelial laser injury. Platelets were stained with intravenous injection of anti-CD49b (Movie 2). Scale bars, 50 μm. (**B**) Open-pouch IVM. Dashed circles represent transmesothelial laser injury. Macrophages were stained with intraperitoneal injection of anti-F4/80 (Movie 2). Scale bars, 50 μm. (**C**) Quantification of aggregate and clot volume in (A) and (B) over time. (**D**) 3D reconstruction of open-pouch IVM model images acquired 30 min after laser injury (Movie 2). Injury size (dashed circle) was increased to span the transmesothelial and transendothelial compartments at the same time. Macrophages were stained by intraperitoneal anti-F4/80 injection; platelets were stained by CD41-YFP fluorescent reporter. Scale bar, 50 μm. (**E**) Platelet and macrophage aggregation traces (recording time = 6 min). The aggregometer was equilibrated with isolated platelets or peritoneal macrophages. After 1 min, agonists were added. A representative image of two independent experiments is depicted. (**F**) Macroscopic image of cuvettes at 10 min. (**G** and **H**) Phase-contrast microscopy of cuvette content at 10 min. Scale bars, 50 μm. Images and curves denote single mice, representative of $N \geq 2$ independent experiments. Auto, autofluorescence.

(P- and L-selectin; fig. S4C), had no effect (fig. S4D). We also tested the most abundantly expressed Ig-like adhesion molecules (Icam2 and CRIg; fig. S4E). Neither *Icam1/Icam2* double knockouts nor *Vsig4* (CRIg) knockouts showed impaired aggregation (fig. S4F). We next investigated expressed genes listed under the gene ontology term "adhesion." The resulting list of candidate molecules was further filtered for proteins localized on the plasma membrane of peritoneal macrophages. In addition to the aforementioned proteins, this approach uncovered the following targetable molecules: CD9, amyloid precursor protein (APP), and thrombospondin 1 (THBS1). APP has previously been reported to mediate neuronal adhesion, whereas THBS1 causes platelet adhesion. However, antibody blockade or genetic deletion of these molecules did not show any significant reduction in the number of macrophages at the injury site when compared to results for the respective wild-type or isotype controls (fig. S4, G to I).

We then hypothesized that molecules not canonically associated with cell-cell adhesion may be involved. Previous studies demonstrated that intraperitoneal administration of heparin inhibited the macrophage disappearance reaction in response to either an intraperitoneal hypersensitivity reaction (*15*) or an infectious agent such as *Escherichia coli* (*11*). In our system, intraperitoneal heparin injection significantly reduced the number of cells attaching to the sterile injury (Fig. 3A and fig. S4J). However, unlike in the aforementioned studies, the use of direct thrombin inhibitors hirudin and argatroban did not replicate this effect (Fig. 3A). Therefore, we tested for thrombin-independent activity of heparin. First, we investigated a role of the alternative pathway of the complement system, which has been described as inhibited by heparin (*16*). However, *C3*-knockout mice did not show a difference compared to wild-type mice (fig. S4I). Heparin is a large polyanion and, as such,

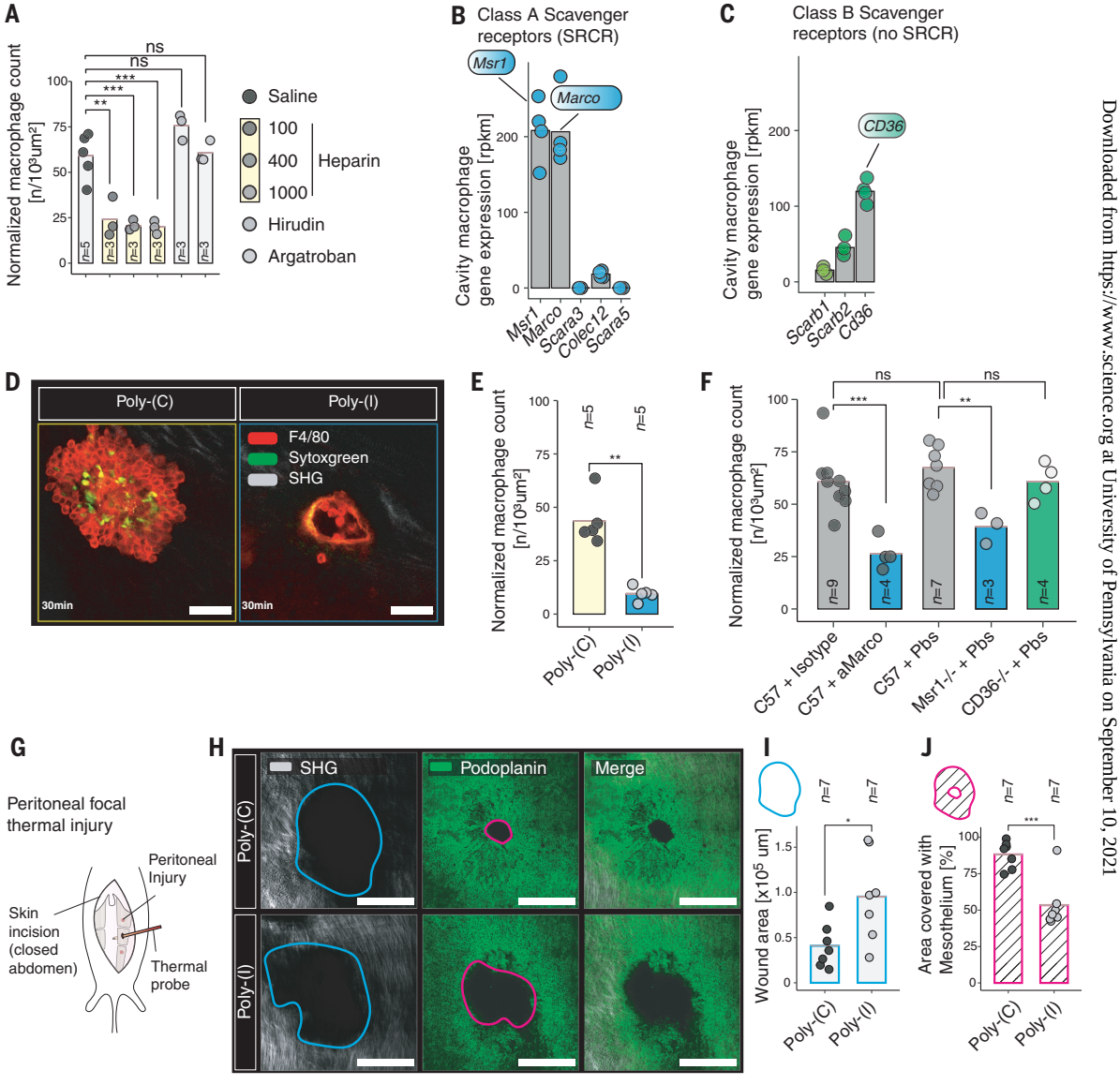

Fig. 3. Aggregation of cavity macrophages does not rely on known mammalian cell-adhesion molecules but relies on evolutionary conserved scavenger receptors. (**A**) Normalized macrophage count (cell count divided by injury size) 30 min after injury. ANOVA: $P < 0.001$, F value = 24.3. (**B** and **C**) RNA sequencing (RNA-seq) gene expression levels ($n = 4$ biological replicates) of class A and class B scavenger receptors, respectively. (**D**) Open-pouch IVM. Images acquired 30 min after transmesothelial laser injury. Animals were treated with either poly(C) or poly(I). Scale bars, 50 μm. (**E**) Normalized macrophage count 30 min after injury, following poly(C) and poly(I) treatment as representatively shown in (D). t test: $t = 6.26$, $P = 0.002$. (**F**) Normalized macrophage count at 30 min after injury. Blocking antibodies were administered 20 min before injury. ANOVA: $P < 0.001$. F value = 11.0. (**G**) Illustration of peritoneal focal thermal injury model. (**H**) Peritoneal flap IVM 3 days after peritoneal focal thermal injury. Animals were treated with either poly(C) or poly(I). Images are representative of quantification shown in (I) and (J). Scale bars, 500 μm. (**I** and **J**) Quantification of wound area (I) and mesothelial coverage (J) 3 days after injury. Data are mean ± individual values (mice). (I) t test: $P = 0.028$, $t = -2.63$; (J) t test: $P = 0.00098$, $t = 4.75$. P values were determined by unpaired t tests or one-way ANOVA with Tukey's post hoc test: $^*P < 0.05$, $^{**}P < 0.01$, $^{***}P < 0.001$, ns $P \geq 0.05$. Data are representative of $N = 2$ independent experiments. rpkm, reads per kilobase of transcript per million mapped reads.

has many thrombin-independent anti-adhesive properties. Thus, we hypothesized that heparin inhibited macrophage adhesion and aggregation by neutralizing receptors that recognize charged motifs.

Murine scavenger receptors initially identified as macrophage receptors that recognize acetylated low-density lipoprotein (*17*) contain scavenger receptor cysteine-rich (SRCR) domains and indiscriminately bind hundreds of different polyanionic ligands (*18*). An SRCR superfamily protein was discovered as a cell-cell adhesion molecule in sea sponges (*19*), and an estimated 1200 SRCR-containing homologs are expressed by sea urchin coelomocytes (*4*, *20*–*22*). Murine cavity macrophages express four SRCR-containing murine homologs, two of which are classified as class A scavenger receptors—the macrophage scavenger receptor 1 (MSR1) and the macrophage receptor with collagenous structure (MARCO) (Fig. 3B). For comparison, we examined CD36, a class B scavenger receptor without SRCR domains that is expressed at similar levels by murine cavity macrophages (Fig. 3C). Although *Cd36*-deficient mice exhibited normal aggregation of macrophages (Fig. 3F), blocking scavenger receptors with the negatively charged molecule polyinosinic acid [poly(I)] significantly decreased macrophage aggregation at the injury (Fig. 3, D and E). Polycytidylic acid [poly(C)] served as a control. Furthermore, specific targeting of MARCO or *Msr1* significantly reduced the number of aggregating cells when compared with their respective controls (Fig. 3F). To determine whether these receptors mediated the initial attachment to the wound or aggregation of the macrophages, we used in vitro aggregometry to directly examine the latter. Poly(I) prevented macrophage aggregation in vitro (fig. S5, A and B). Next, using our intravital imaging setup, we examined aggregate formation over time after poly(I) administration and observed a significant decrease in macrophage-macrophage aggregate formation while the initial adhesion to the wound was left relatively intact (Fig. 3D). Thus, scavenger receptors in this system are not required for the initial (cell-matrix) attachment to the wound. Rather, they serve as secondary tethers during the second step, macrophage (cell-cell) aggregation.

A comparison of *Marco* and *Msr1* transcriptomic expression across many macrophage populations in a previously published dataset (*23*) revealed *Marco* expression exclusively in peritoneal and liver macrophages but not in adipose tissue, colon, pancreatic islets, brain, or blood monocytes (fig. S5C). *Msr1* was expressed in most populations of macrophages, but expression in peritoneal macrophages was significantly higher than in other populations studied (fig. S5D). In addition to detecting these receptors on the surface of the peritoneal GATA6^{+} macrophages, activation of these cells with ATP resulted in rapid (30 min) mobilization of MARCO and MSR1 from an intracellular pool to the membrane in vitro (fig. S5, E and F).

Next, we examined the functional consequences arising from the inhibition of cavity macrophage aggregation. A focal thermal injury of the parietal peritoneum through an intact abdominal wall showed prolonged healing when macrophage aggregation was blocked with poly(I), which suggests that aggregate formation functionally aided the healing process (Fig. 3, G to J). Focal thermal lesions of

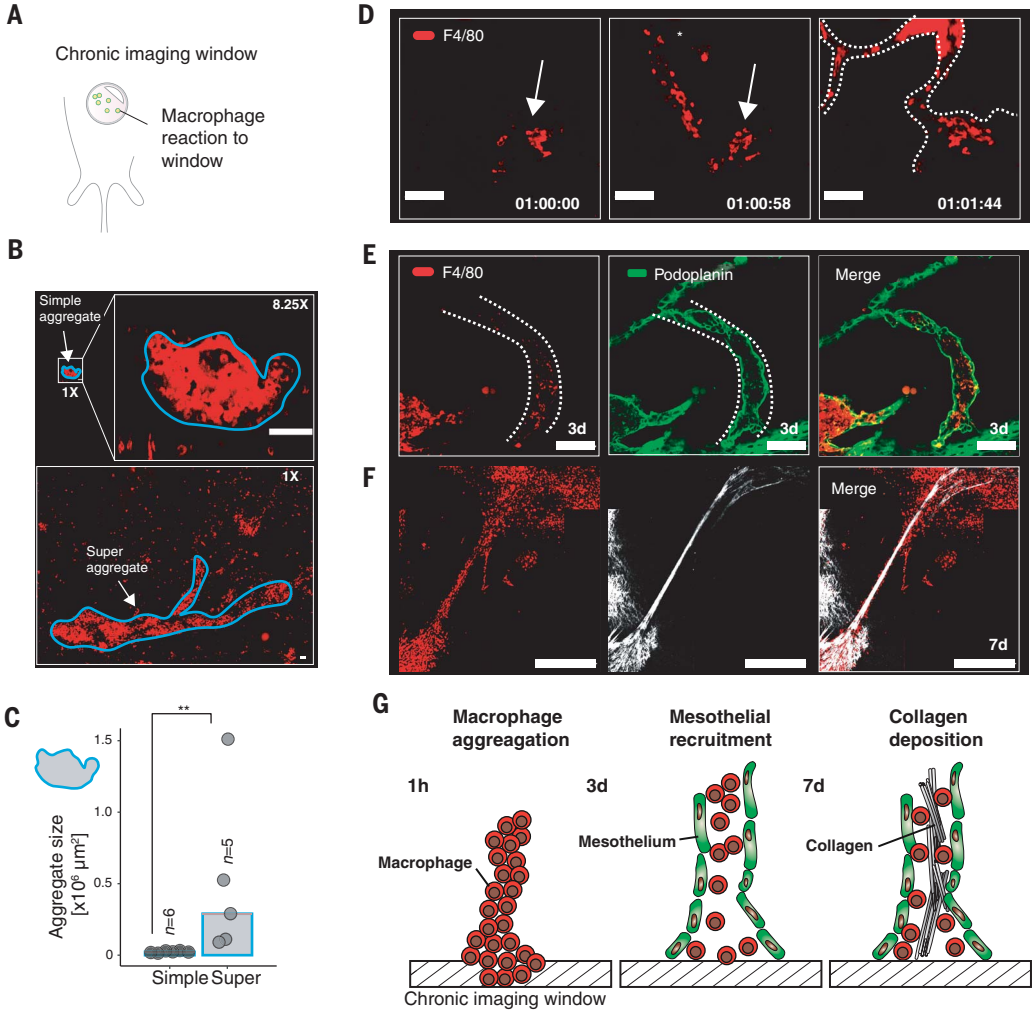

Fig. 4. Super-aggregates and scar formation. (**A**) Illustration of abdominal-window IVM (AW-IVM). (**B**) Size comparison of an open-pouch (simple) macrophage aggregate versus an AW-IVM (super) macrophage aggregate. Scale bars, 50 µm. (**C**) Quantification of representative images shown in (B). Wilcoxon test: $P = 0.004$. (**D**) AW-IVM 1 hour after window implantation. Macrophages were stained with intraperitoneal injection of anti-F4/80. Over time, macrophages attached to the window (arrows) merged with macrophages attached to an intra-abdominal organ (asterisk) to form super-aggregates (i.e., adhesion precursors; dashed lines) (Movie 3). Scale bars, 100 µm. (**E**) AW-IVM 3 days after window implantation. Macrophages and mesothelium were stained with intraperitoneal injection of anti-F4/80 and anti-podoplanin, respectively. Dashed lines indicate adhesions. Scale bars, 100 µm. (**F**) AW-IVM 7 days after window implantation. Scale bars, 500 µm. (**G**) Illustration of (D) to (F). SHG visualizes de novo collagen deposition. Data are median ± individual values (mice). *P* values were determined by Wilcoxon test: $^{**}P < 0.01$. Data are representative of $N = 2$ independent experiments.

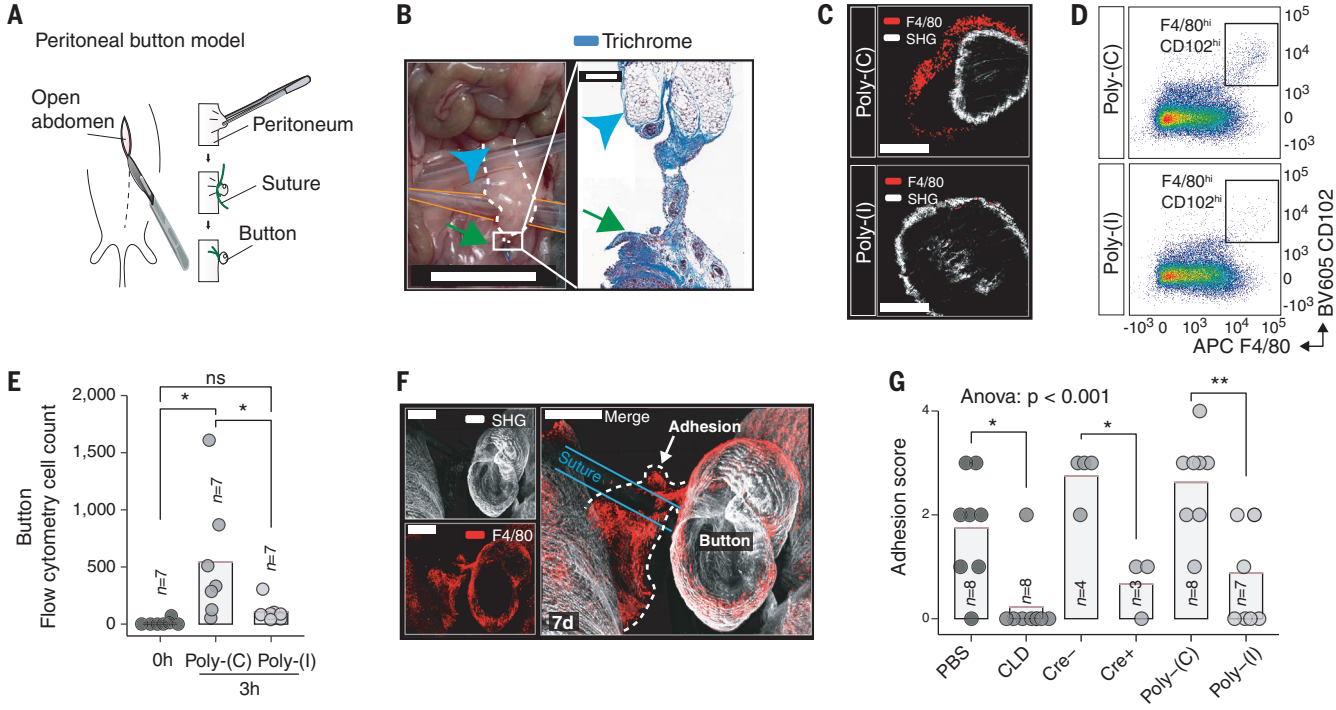

Fig. 5. Clinical implications of macrophage aggregation inhibition. (**A**) Illustration of peritoneal button injury model. (**B**) Macroscopic and microscopic images of peritoneal adhesion (dashed lines) 7 days after peritoneal button injury. Adhesion ranges from the peritoneal button (arrows) to the omentum (arrowheads). A yellow pipette tip (orange lines) was inserted below the adhesion. The microscopic image shows a section stained with Masson's trichrome. Scale bars, 1 cm (macroscopic) and 300 μm (microscopic). (**C**) Cleared whole-mount microscopy images of peritoneal buttons, harvested 7 days after surgery. Scale bars, 200 μm. (**D**) Representative flow cytometry scatter plots, pre-gated on size, singlet, live $CD45^+CD3^-CD19^-$. (**E**) Quantification of peritoneal macrophages ($F4/80^{hi}CD102^{hi}$) as representatively shown in (D). ANOVA: $P = 0.013$, F value = 5.48. (**F**) Whole-mount microscopy of peritoneal button and peritoneal adhesion 7 days after surgery. Blue lines indicate the position of sutures. Scale bars, 500 μm. (**G**) Quantification of peritoneal adhesions 7 days after surgery. ANOVA: $P < 0.001$. PBS, phosphate-buffered saline liposomes; CLD, clodronate liposomes; Cre^+, $Csf1R^{Cre+}$iDTR; Cre^-, $Csf1R^{Cre-}$iDTR; iDTR, inducible diphtheria toxin receptor. Data are mean ± individual values (mice). P values were determined by ANOVA with Tukey's post hoc test: $^*P < 0.05$, $^{**}P < 0.01$, ns $P \geq 0.05$. Data are representative of $N = 2$ independent experiments.

peritoneal organs such as liver, with minimal opening of the cavity, were similarly affected (fig. S6, A to D). In animals that did not receive poly(I), no lesions on the liver or abdominal wall were observed after 14 days, and healing occurred without intra-abdominal scars, thus demonstrating the capacity to fully heal these lesions without a scarring phenotype.

Pathologic scarring mediated by Gata6$^+$ macrophages

In echinoderms, the response to body wall injury includes the formation of an aggregate of coelomocytes and local production of collagen material (*3*, *24*). In humans, intra-abdominal scars frequently occur after abdominal surgery, manifesting as peritoneal adhesions. Peritoneal adhesions are defined as irreversible bands of scar tissue that attach abdominal structures at non-anatomic locations (*25*). Peritoneal adhesions are a major health burden for patients, leading to potentially life-threatening intestinal occlusion (*25*, *26*, *27*) and more than 300,000 additional abdominal operations per year in the United States alone, costing several billion dollars annually (*28*). In addition, peritoneal adhesions remain an unresolved clinical challenge that, to date, lacks effective treatment. We therefore investigated whether the aggregation of mammalian cavity macrophages in response to injury could lead to the formation of peritoneal adhesions. Using a chronic imaging window that required the opening of the peritoneal cavity (Fig. 4A), we observed that macrophages aggregated within minutes on either the window surface (fig. S1A) or the surface of adjacent abdominal organs (fig. S7A) or formed free-floating aggregates (fig. S7B). Subsequently, macrophage aggregates began to merge and form super-aggregates. The super-aggregates that formed in response to implantation of an imaging window were up to 100 times the size of the simple aggregates that formed in response to peritoneal laser injury (Fig. 4, B and C). Super-aggregates began to form bridges between the imaging window and intra-abdominal organs such as the omentum (Fig. 4D, Movie 3, and movie S5) or the small intestine (fig. S7C and movie S6). Macrophage super-aggregates were covered with a mesothelial lining within 3 days (Fig. 4E). After 7 days, but not earlier, collagen was deposited within these macrophage super-aggregates (Fig. 4F and fig. S7, D and E). Both coverage with mesothelium and deposition of collagen are considered hallmarks of peritoneal adhesion formation (*25*). Thus, a severe iatrogenic disturbance of the peritoneal compartment, such as a laparotomy and introduction of a foreign body, can result in exaggerated and dysregulated aggregation of cavity macrophages. The resulting super-aggregates are then precursors of peritoneal adhesions.

To quantify peritoneal adhesion formation in a system with more clinical relevance, we used a previously described model of surgical sterile injury: the peritoneal button model (*29*, *30*). In this model, a laparotomy (midline) is generated and a portion of the peritoneal wall—including both the muscle layer and peritoneal membrane—is grasped with forceps and ligated at its base, creating a button in each quadrant of the peritoneal cavity (Fig. 5A). In comparison with the focal thermal injuries, which heal without scar formation, this model provides a more iatrogenic setting with laparotomy, creation of ischemic pockets, and the

introduction of foreign material (polypropylene suture). The model led to the reproducible formation of peritoneal adhesions (scars) between the buttons and adjacent intra-abdominal organs within 7 days (Fig. 5B). Within 3 hours after surgery, aggregates of cavity macrophages were recruited from the peritoneal fluid to the buttons (Fig. 5, C to E), a process that could be reduced when scavenger receptors were blocked with poly(I) (Fig. 5, C to E). A significant number of cavity macrophages engaged in this process, as their numbers were greatly reduced in the peritoneal lavage after surgery, a process that was only partially inhibited with poly(I) (fig. S8, A and B). Notably, peritoneal adhesions harvested 7 days after surgery often formed at the sutures used to create the peritoneal buttons (Fig. 5F) and were full of macrophages, with the highest concentration around the polypropylene sutures (Fig. 5F). The number and tenacity of peritoneal adhesions that formed within 7 days after surgery was significantly reduced after both depletion of cavity macrophages and blockage of macrophage recruitment by inhibiting scavenger receptors with poly(I) (Fig. 4G). Notably, neutrophils were also recruited to the peritoneal buttons after 4 hours (fig. S7F), reflecting their response to injury. However, the depletion of neutrophils had no effect on adhesion formation (fig. S7G).

Discussion

Primitive organisms such as the sea urchin are entirely dependent on innate immunity to combat pathogens and tissue injury. The coelomocytes in these organisms appear to perform antimicrobial immunocyte functions but also rapidly plug punctures that would otherwise fatally disrupt homeostasis. We show herein that mammals have retained these primordial immune cells with hybrid platelet-macrophage properties to ensure extremely rapid healing responses. Although numerous groups have reported that platelets retain some immune function (*31*–*34*), we now report that the GATA6$^+$ macrophages—likely in all cavities—retain important platelet-like functions. Integrins mediate most adhesion processes in immune cells. However, most of these molecules, with the exception of platelet integrins, fail to function under high-shear conditions (*35*). The class A scavenger receptors are characterized by an evolutionarily conserved SRCR domain, a motif of 90 to 110 amino acids with several cysteine residues (*36*), that mediates charge interactions. These domains are thought to play critical roles in organisms such as the purple sea urchin, which possesses more than 1200 SRCR domains (*22*). Notably, the SRCR superfamily is highly conserved in vertebrates (*20*, *21*). For example, the SRCR domain of Msr1 (SR-A) is 78% conserved between mammalians and *Xenopus tropicalis* (western clawed frog) (*21*). Within the SRCR domain of Marco, the RGRAEVYY motif (R, Arg; G, Gly; A, Ala; E, Glu; V, Val; Y, Tyr) is highly conserved across mammals (*21*). To date, these receptors have been considered to perform critical scavenging functions. In this work, we describe an important function of scavenger receptors in primordial GATA6$^+$ macrophages: a key role in macrophage aggregation as part of a recruitment pathway that leads to repair of focal peritoneal injuries. It is likely that the scavenger receptors on each of two macrophages bind the same negatively charged polyanions (e.g., chemically modified lipoproteins, acidic phospholipids, numerous polysaccharides, and polyribonucleotides) that then bridge the cells as secondary tethers. We hypothesize that these focal perturbations reflect a type of injury that the immune system has been challenged with throughout evolution. However, iatrogenic procedures such as abdominal surgery, which include exposure to the external environment and potential implantation of foreign material, reflect a type of injury that appears to have no evolutionary precedent (*37*). In this scenario, peritoneal macrophages may cause detrimental scarring in an inadvertent attempt to repair tissue ad integrum. Thus, inhibition of macrophage scavenger receptors may provide a target for prevention of scar formation after surgery in the peritoneal cavity and perhaps other cavities that contain these cells.

Materials and methods

Mice

All mice were maintained on the C57BL/6 background. *Gata6*$^{H2B\text{-}Venus/+}$ mice (*38*) (MGI Ref. ID: J:226600) were a gift from A. K. Hadjantonakis (Memorial Sloan Kettering, NY). *LysM*$^{eGFP/+}$ mice (*39*) (MGI Ref. ID: J:63254) were a gift from T. Graf (Albert Einstein University, NY), *Ly6G*$^{Cre\text{-}tdTomato}$ catchup mice (*40*) (MGI Ref. ID: J:227159) were kindly provided by S. Lacroix (Université Laval, QC, Canada, with permission from M. Gunzer). *CD41*$^{YFP/+}$ mice (*41*) (MGI Ref. ID: J:123159) were a gift from K. McNagny, University of British Columbia, Vancouver, BC, Canada. *Icam1/2*$^{-/-}$ mice were a gift from R. Alon (Weizmann Institute of Science, Israel). *Icam1/2*$^{-/-}$ mice were generated by mating *Icam1*$^{-/-}$ (MGI Ref. ID: J: 18743) and *Icam2*$^{-/-}$ (MGI Ref. ID: J:54748) mice. *Crig*$^{-/-}$ mice (*42*) (MGI Ref. ID: J:138691) were a gift from M. van Lookeren Campagne (Genentech, San Franscisco, CA). *Csf1R*$^{HBEGF/mCherry}$ mice (Jax: 024046) were crossed with *LyzM*^{Cre} (Jax: 004781) as previously described (*43*) generating Cre$^+$ and Cre$^-$ littermates. Wild-type C57BL/6, *C3*$^{-/-}$ (Jax: 3641), *Msr1*$^{-/-}$ (Jax: 006096), *CD36*$^{-/-}$ (Jax: 019006), *Thbs1*$^{-/-}$ (Jax: 006141) and *App*$^{-/-}$ (Jax: 004133) were purchased from Jackson laboratories. Animals were maintained in a specific pathogen-free double-barrier unit at the University of Calgary Animal Resource Centre. Mice were fed autoclaved rodent feed and water ad libitum. Male and female mice with an age between 8 and 12 weeks were used for experiments. Experimental animal protocols used in this study were approved by the Health Science Animal Care Committee of the University of Calgary (Reference number AC19-0138) and were in compliance with the guidelines from the Canadian Council for Animal Care.

Antibodies and reagents

The following monoclonal antibodies and reagents were used for intravital microscopy staining: PE-conjugated anti-mouse F4/80 (0.8 μg per mouse intraperitoneally, BM8, BioLegend); PE-conjugated anti-mouse CD49b (1.6 μg per mouse intravenously, HMα2, BD); Alexa Fluor 488-conjugated anti-mouse podoplanin (4 μg per mouse intraperitoneally, eBio8.1.1, eBioscience). Sytox green nucleic acid stain (0.2 μl per mouse intraperitoneally, 5 mM stock solution, Invitrogen).

The following neutralizing antibodies (versus isotype controls) and reagents were intraperitoneally tested for their effect on macrophage recruitment: anti-mouse CD18 (100 μg per mouse, GAME-46, BD Pharmingen) + anti-mouse CD29 (100 μg per mouse, HM β1-1, BD Pharmingen) versus isotype rat IgG1, κ (100 μg per mouse, BioXcell) + hamster IgG (100 μg per mouse, eBioscience); anti-mouse CD162 (100 μg per mouse, 4RA10, BD Pharmingen) versus isotype rat IgG1 (100 μg per mouse, eBioscience); anti-human CD9 (10 μg per mouse, ALB 6, Santa Cruz) versus isotype mouse IgG1 (BD Biosciences). Heparin (Sandoz) was diluted in sterile saline to reach final dose of 100 to 1000 U per mouse. Argatroban (Sigma-Aldrich) was dissolved in DMSO at 20 mg/ml and diluted with saline to reach a final concentration of 300 μg per mouse. Hirudin (Multiplate Hirudin Blood Tube, Roche) was dissolved in saline and injected intraperitoneally at a dose of 1 tube per mouse. Polyinosinic acid [poly(I)] and policytidylic acid [poly(C)] were purchased as potassium salt (Sigma-Aldrich) and dissolved in double-distilled water according to manufacturer's instructions to 5 mg/ml and 20 mg/ml, respectively. Immediately before experiments, the poly(C) stock solution was diluted with double-distilled water to a final concentration of 5 mg/ml. Both poly(I) and poly(C) were then diluted with saline to reach a final dose of 250 μg per mouse. A total of 125 mg of anti-mouse Marco antibody (ED31, Biorad MCA1849) versus rat IgG1 isotype control (eBRG1, eBioscience 16-4301-85) was injected intraperitoneally in a total volume of 140 μl of PBS per mouse. A 100-μl volume anti-mouse thrombocyte depletion serum (Cedarlane, CLAD31440) versus normal rabbit serum

(Cedarlane, CLSD403) was injected intravenously 24 hours before imaging.

Antibodies, dyes, and their concentrations used for flow cytometric analysis of peritoneal lavage are summarized in table S2.

The following reagents were intraperitoneally injected at 24 hours before surgery for their effect on post-surgical adhesion formation: Diphtheria toxin from *Corynebacterium diphtheriae* (5 ng per gram of body weight, in *Csf1r*^{Cre} iDTR mice) or clodronate- or PBS-loaded liposomes (100 μl per mouse, clodronateliposomes.com).

Multiphoton intravital microscopy (IVM)

Mice used for IVM were 8 to 10 weeks old weighted an average of 20 g. Mice in each experiment were of the same sex. If not specified otherwise, mice were generally treated pharmacologically or with neutralizing antibodies 20 min before imaging. Mice were anesthetized with a mixture of ketamine hydrochloride (200 mg/kg, Rogar/SBT) and xylazine hydrochloride (10 mg/kg, MTC Pharmaceuticals). After anesthesia, the tail vein was cannulated for administration of additional anesthetic, antibodies, or other reagents in certain experiments.

Pouch-model IVM (Fig. 1) was prepared with the mouse in supine position. Thermal support was provided with a heated stage to maintain body temperature at 37°C. The fur and skin above the ventral abdominal wall were aseptically cleaned with 70% ethanol and then removed. Care was taken not to open the peritoneal cavity. If the peritoneal cavity was accidentally opened, the mouse was immediately euthanized. Staining antibody or dye was intraperitoneally injected with a 28G needle in midline about 10 mm above the symphysis. After withdrawing the needle, a suture was placed to seal the hole caused by the injection. This suture was then used to immobilize a part of the peritoneum onto the coverslip. For this, the mouse was placed in a semi-prone position. Placing a cotton tip with slight top to bottom pressure helped to further increase imaging stability yet preserved a connection between the imaging pouch and peritoneal cavity so that peritoneal fluid movement was preserved. The closed pouch was prepared by applying more pressure on the cotton tip which allowed us to separate the pouch from the peritoneal cavity in terms of fluid movement. After IVM, all mice were immediately euthanized.

Abdominal-wall-flap IVM was used to visualize the mesothelium and epigastric blood vessels (Fig. 2A and Fig. 3, F to I). Mice were placed in supine position on a heated stage to maintain body temperature at 37°C. The fur and skin above the ventral abdominal wall were removed and then aseptically cleaned with 70% ethanol. Staining antibodies (anti-mouse podoplanin and anti-mouse F4/80 as described above) were injected. After mice were incubated for 10 min on a heated stage, the peritoneum was incised with an inverted U-shaped incision ranging from directly below the xyphoid process to the inguinal ligament on both sides. This created a perfused flap of peritoneum and the rectus abdominis muscles. The flap was washed with 1 ml of PBS and placed directly on the glass coverslip of the heated stage for imaging of abdominal wall or epigastric blood vessels.

Intravital liver imaging was performed as previously described (*44*). Exposed tissues were visualized with a Leica SP8 DIVE inverted microscope equipped with 4Tune, a tunable in vivo detection system and a multiphoton light path. All images shown here were acquired using a HC FLUOTAR L 25X/0.95 W objective with water as immersion medium and 2X digital zoom. Fluorescent moieties were excited with a tunable InSight X3 ultrafast laser (Spectra-Physics) at 800 to 1000 nm. Signal was detected using external, extremely sensitive non-descanned hybrid detectors. Second-harmonic generation by collagen was recorded by tuning the detector to excitation wavelength divided by 2 ± 20 nm. Leica LAS X software was used to drive the microscope.

In vivo interventions

For surgical procedures, mice were 8 to 12 weeks old with a body weight >20 g. Mice in each experiment were of the same sex. Mice were treated before surgery with poly(I), poly(C), liposomes, or diphtheria toxin as described above. Anesthesia was induced and maintained with isoflurane. Eye lubricant was topically applied and buprenorphine (0.1 mg/kg) was subcutaneously administered.

The peritoneal focal thermal injury was adapted from the focal thermal liver injury that was previously described (*45*). The skin was incised in midline. Care was taken not to injure the peritoneum or open the peritoneal cavity. The peritoneum was lifted in midline and three focal injuries were induced through the rectus abdominus muscle using the tip of a heated 30G needle mounted on an electrocautery device. Finally, the skin was sutured with 6-0 Prolene (Ethicon) running suture.

For the peritoneal button injuries, skin was incised in midline. The peritoneal cavity was accessed through midline laparotomy. Standardized lesions were induced as previously described (*46*). In brief, a small portion of the peritoneum was grasped and ligated at its base using 4-0 Prolene suture (Ethicon), creating a standardized peritoneal button. This was repeated for a total of four buttons, one in each quadrant. Finally, peritoneum and skin were sutured with 6-0 Prolene (Ethicon) running suture.

The abdominal imaging window (fig. S1 and Fig. 4) was manufactured and implanted as previously described (*47*). In brief, a round cover glass was mounted on a custom-made titanium ring and sterilized in ethanol. A midline laparotomy was performed and a purse-string suture (5-0 Vicryl Rapide, Ethicon) was placed in a circular fashion along the whole incision. Then, the cover-glass titanium ring was inserted and the suture was tightened, securing the titanium ring in place and hermetically sealing the abdominal cavity from the exterior. Mice were monitored for weight loss and repetitively imaged for up to 7 days.

Focal thermal injury in the liver was performed as previously described (*48*). In brief, a mini-laparotomy was performed just below the xyphoid to expose the liver. Three focal injuries were induced on the surface of the liver using the tip of a heated 30G needle mounted on an electrocautery device. The incision was sutured closed, and animals could recover for imaging of indicated time points after injury.

For bone marrow chimera generation, 6-week-old female C57BL/6J mice were lethally irradiated (2×525 cGY) and subsequently reconstituted with *Gata6*H2B-Venus bone marrow cells for 8 weeks.

Peritoneal fluid volume estimation

Urea nitrogen diffuses freely between the peritoneal cavity and the serum with a very fast equilibration time (*49*). Therefore, we assume that blood urea nitrogen [BUN] and peritoneal fluid urea nitrogen [PerUN] concentrations are in equilibrium: [BUN] ≈ [PerUN]. During harvesting, the peritoneal cavity was flushed with a known volume (V_{wash}), diluting the original peritoneal fluid of unknown volume (V_{per}). The concentration of urea nitrogen in the blood [BUN] and in the peritoneal lavage [WashUN] was determined using a calorimetric detection kit (Invitrogen, #EIABUN) according to the manufacturer's instructions. Based on the formula: [PerUN] × V_{per} = [WashUN] × V_{wash}, the peritoneal fluid volume was estimated, by substituting [PerUN] with [BUN]: $V_{per} = V_{wash} \times$ [WashUN]/[BUN].

Adhesion scoring, whole-mount imaging, and tissue clearing

Prior to euthanasia, mice were anesthetized (10 mg/kg xylazine hydrochloride and 200 mg/kg ketamine hydrochloride). Laparotomies were performed in an inverted U shape. Adhesion were scored based on their tensile strength and vascularization (table S1) as previously described (*50*). The animal was subsequently euthanized and perfused with 2 mM EDTA and 4% PFA containing PBS. Peritoneal buttons/adhesions were excised and post-fixated in 4% PFA containing PBS for 2 to 4 hours. Tissue staining and clearing was performed as previously described (*51*). In brief, fixed biopsies were washed and permeabilized three times

for 30 min in 1% Triton X containing PBS and subsequently blocked two times for 1 hour in 1% Triton, 10% FBS, and 0.02% sodium azide containing PBS. Then the biopsies were incubated with fluorescently conjugated monoclonal antibodies for 1 to 4 days at 4°C on a rotation device. Samples were then washed three times for 1 hour in 1% Triton X containing PBS followed by sequential dehydration steps (50%, 70%, 99%, and 99% EtOH) for 4 hours at 4°C. After dehydration, the buttons were placed in ethyl cinnamate (Sigma). For imaging, cleared biopsies were placed in an ethyl cinnamate containing vessel with the suture facing downward. Image acquisition was performed using a Leica TCS SP8 inverted multi-photon laser-equipped microscope. All images shown here were acquired using a HC FLUOTAR L 25X/0.95 W objective with water as immersion medium. Fluorescent moieties were excited with a tunable InSight X3 ultrafast laser (Spectra-Physics) at 800 to 1000 nm. Signal was detected using external, non-descanned hybrid detectors. Second-harmonic generation by collagen was recorded by tuning the detector to excitation wavelength divided by 2 ± 20 nm. Leica LAS X software was used to drive the microscope.

Cell isolation and flow cytometry

Mouse peritoneal lavage was performed in anesthetized animals by injection and aspiration of three times 5 ml of sterile ice-cold PBS containing 2 mM EDTA into the peritoneal cavity and subsequent retrieval. Lavage samples were subsequently centrifuged at 500*g* for 5 min at 4°C and the cell pellet was subsequently processed for flow cytometry. Peritoneal buttons were excised and subsequently digested in 125 U/ml collagenase IV (Worthington Biochemical), 60 U/ml DNaseI (Roche) containing HBSS for 30 min in a 37°C water bath with repetitive shaking. Homogenates were initially passed through a 70-μm cell strainer and spun down at 500*g* for 5 min at 4°C and cell pellet was directly processed for flow cytometry. The cells were incubated in protein based live/dead stain (table S2) and blocked using anti-mouse CD16/32 antibody (2.4G2 clone, BioXcell) for 20 min. Cells were incubated for 20 min with fluorescently labeled antibodies (table S2). Samples were run using BD FACS Canto flow cytometer and analyzed using FlowJo software (Tree Star). Gata6$^+$ cavity macrophages were pre-gated on singlet, live CD45$^+$ CD19$^-$CD3$^-$Ly6G$^-$CD11b$^+$ and then identified as F4/80^{hi}CD102$^+$.

Activation of peritoneal macrophages

To study cell activation mouse peritoneal lavage was performed as described above. Cells were spun down and resuspended in RPMI medium (37°C). Then, 100 μM ATP and 2 mM calcium (treatment group) or 2 mM calcium only (negative control) was added. Tubes containing cells were then incubated in the cell-culture incubator with the leads open for 30 min. The cells were then centrifuged at 500*g* for 5 min and washed twice with cold PBS. Half of the samples were cells were permeabilized using the BD Fixation/Permeabilization Kit according to the manufacturer's instructions (BD Biosciences). Cells were incubated with fluorescently labeled antibodies (table S2) and the appropriate fluorescence minus one (FMO) controls. Samples were run using BD FACS Canto flow cytometer and analyzed using FlowJo software (Tree Star). Gata6$^+$ cavity macrophages were pre-gated on singlet, live CD45$^+$Ly6G/C$^-$CD11b$^+$ cells. The mean fluorescence intensity of Msr1 and Marco for both permeabilized and unpermeabilized cells was measured on F4/80^{hi}CD102$^+$ cells. Cytosolic expression was estimated by subtracting surface expression (non-permeabilized) from total expression (permeabilized).

Aggregometry

Macrophages were isolated by peritoneal lavage as described above with the use of 2 mM EDTA containing HBSS instead of PBS. Macrophages were centrifuged at 300*g* for 5 min in a 50-ml polystyrene tube. The pellet (with approximately 100 μl of fluid remaining with 3×10^6 cells) was diluted in HBSS containing 2 mM Ca^{2+} to a final volume of 400 μl. The cell suspension was then transferred to a aggregometry cuvette, which was warmed to 37°C and continuously stirred (400 rpm). Light transmission was recorded on a 700 Whole Blood/Optical Lumi-Aggregometer (Chrono-log) and was expressed in arbitrary units with buffer representing 100% transmission and washed macrophage suspension 0% transmission, respectively. Agonists and calcium were added to reach a Ca^{2+} concentration of 4 mM total or 2 mM free calcium in a buffer containing 2 mM EDTA. The preparation of platelet aggregometry was performed as previously described (*52*). Washed platelets (50 μl with 5×10^5 platelets per microliter) were diluted into 110 μl of Tyrode-HEPES buffer containing 2 mM Ca^{2+} and 100 μg/ml human fibrinogen. Agonists (ATP, thrombospondin) were added at the indicated concentrations to the continuously stirred platelet suspension. Murine neutrophils were isolated from the bone marrow of wild-type C57Bl/6, mice as previously described (*45*). Briefly, bone marrow was collected from the femurs and tibias of euthanized mice, and neutrophils were isolated using a discontinuous Percoll gradient consisting of a Percoll solution (9 ml of Percoll and 1 ml 10X of HBSS) diluted to 72%, 64%, and 52% in 1X HBSS. Following centrifugation, the neutrophil band was removed and washed in HBSS. Cell pellets were resuspended in HBSS containing either 2 mM Ca^{2+} or EDTA. Aggregometry was performed as described above.

Analysis of RNA-seq data

The dataset used to probe gene expression or peritoneal cavity macrophages was previously published (*14*) and is accessible on the gene expression omnibus (GEO) database (GSE131724). In this study, peritoneal cavities of 8-week-old C57BL/6 mice were lavaged. The F4/80^{hi} CD102$^+$ cells were sorted and underwent bulk RNA sequencing. Data were demultiplexed and converted to FastQ using Bcl2fastq 2.17.1.14 (Illumina) and mapped to mm10 with Tophat 2.1.1. RPKM counting and normalization were performed using Partek GS 7.18.0723. Genes of interest were filtered and displayed for manually selected genes and Pathway gene sets from Gene Ontology (GO) biological processes (accessed at www.informatics.jax.org) using the R environment for statistical computing.

The dataset used to compare scavenger receptor expression across macrophages isolated from different tissues was previously published (*23*) and was accessed on the GEO database (GSE133127). Count data were analyzed as previously described (*53*). In brief, raw counts transformed were to log counts per million using the calcNormFactors() and cpm() functions of the edgeR package, after filtering for genes that were not expressed using the function filterByExpr(). Unsupervised clustering was done using the plotMDS() function of the limma package using normalized counts. Differential expression analysis was performed using linear modeling and subsequent Bayes moderation after removing heteroscedascity from count data using voom().

Image analysis

Images were exported as uncompressed .tif files and analyzed using ImageJ (*54*). Tracking was generally performed in an automated fashion using the TrackMate plugin (*55*). The cell shown in Fig. 1J was tracked manually. Cell counts and injury size was measured manually in ImageJ. Three-dimensional visualizations and volume quantifications were performed in Imaris software. Analysis results from ImageJ and Imaris software were exported as .csv files and analyzed/plotted using R statistical environment. Raw images, tracking results, and R scripts to reproduce all figures are available at Dryad (*56*).

Transmission electron microscopy

Aggregation of macrophages was performed as described above. Samples were submerged with fixative witch was prepared as follows: 2.5% glutaraldehyde (Agar Scientific, Stansted, Essex, UK) in 0.15 M HEPES (Fluka, Buchs, Switzerland) with an osmolarity of 670 mOsm and adjusted to a pH of 7.35. The cells remained in the fixative at 4°C for at least

24 hours before further processing. They were then washed with 0.15 M HEPES three times for 5 min, postfixed with 1% OsO4 (EMS, Hatfield, USA) in 0.1 M Na cacodylate buffer (Merck, Darmstadt, Germany) at 4°C for 1 hour. Cells were then washed in 0.05 M maleic NaOH buffer three times for 5 min and dehydrated in 70%, 80%, and 96% ethanol (Alcosuisse, Switzerland) for 15 min each at room temperature. Subsequently, cells were immersed in 100% ethanol (Merck, Darmstadt, Germany) three times for 10 min, in acetone (Merck, Darmstadt, Germany) two times for 10 min, and finally in acetone-Epon (1:1) overnight at room temperature. The next day, cells were embedded in Epon (Sigma-Aldrich, Buchs, Switzerland) and left to harden at 60°C for 5 days.

Sections were produced with an ultramicrotome UC6 (Leica Microsystems, Vienna, Austria): first semithin sections (1 µm) were used for light microscopy, which were stained with a solution of 0.5% toluidine blue O (Merck, Darmstadt, Germany); then ultrathin sections (70 to 80 nm) were used for electron microscopy. The sections were mounted on single slot copper grids and stained with UranyLess and lead citrate with an ultrostainer (Leica Microsystems, Vienna, Austria). Sections were then examined with a transmission electron microscope (Tecnai Spirit, FEI, Brno, Czech Republic) equipped with a digital camera (Veleta, Olympus, Soft Imaging System, Münster, Germany).

Design and statistical analysis

Sample size was determined prior to experiment for all experiments used for hypothesis testing (i.e., data that include statistical inference) except for RNA-seq datasets that were re-analyzed.

Mice receiving pharmacological treatment were randomized. When comparing genetically modified mice, care was taken to alternate between conditions. Investigators were blinded when assessing adhesion scores in the peritoneal button adhesion model. Otherwise, no blinding was performed. Animals that died during experiments were excluded from analysis. If the abdominal cavity was accidentally opened during pouch intravital microscopy, animals were immediately euthanized and excluded from analysis. The number of times the experiment was replicated in the laboratory (N) as well as the number of biological replicates (n) is stated for each experiment in the figure legends. Generally, each data point represents one biological replicate if not explicitly state otherwise in the figure legend (Fig. 1M). All data are presented as mean (bar) + individual values. Statistical comparisons were performed using R statistical environment. Data were compared either by unpaired two-tailed t test or one-way or two-way ANOVA. Non-normally distributed variables were compared using unpaired two-samples Wilcoxon tests. Multiple comparisons were corrected with the Holm-Bonferroni method. A P value of 0.05 was considered the threshold for significance. The underlying raw data and R scripts necessary to reproduce the figures shown in this manuscript are accessible at Dryad (*56*).

REFERENCES AND NOTES

1. H. Chisholm, Ed., "Coelom and serous membranes" in *Encyclopædia Britannica* (Horace Everett Hooper, ed. 11, 1911), vol. 6, pp. 642–644.
2. K. Buchmann, Evolution of Innate Immunity: Clues from Invertebrates via Fish to Mammals. *Front. Immunol.* **5**, 459 (2014). doi: 10.3389/fimmu.2014.00459; pmid: 25295041
3. K. A. Coffaro, R. T. Hinegardner, Immune response in the sea urchin *Lytechinus pictus*. *Science* **197**, 1389–1390 (1977). doi: 10.1126/science.331476; pmid: 331476
4. Z. Pancer, Dynamic expression of multiple scavenger receptor cysteine-rich genes in coelomocytes of the purple sea urchin. *Proc. Natl. Acad. Sci. U.S.A.* **97**, 13156–13161 (2000). doi: 10.1073/pnas.230096397; pmid: 11069281
5. L. C. Smith, L. Chang, R. J. Britten, E. H. Davidson, Sea urchin genes expressed in activated coelomocytes are identified by expressed sequence tags. Complement homologues and other putative immune response genes suggest immune system homology within the deuterostomes. *J. Immunol.* **156**, 593–602 (1996). pmid: 8543810
6. Z. Pancer, J. P. Rast, E. H. Davidson, Origins of immunity: Transcription factors and homologues of effector genes of the vertebrate immune system expressed in sea urchin coelomocytes. *Immunogenetics* **49**, 773–786 (1999). doi: 10.1007/s002510050551; pmid: 10398804
7. B. J. Hillier, V. D. Vacquier, Amassin, an olfactomedin protein, mediates the massive intercellular adhesion of sea urchin coelomocytes. *J. Cell Biol.* **160**, 597–604 (2003). doi: 10.1083/jcb.200210053; pmid: 12591917
8. P. T. Johnson, The coelomic elements of sea urchins (Strongylocentrotus). I. The normal coelomocytes; their morphology and dynamics in hanging drops. *J. Invertebr. Pathol.* **13**, 25–41 (1969). doi: 10.1016/0022-2011(69)90236-5; pmid: 5775463
9. E. E. Ghosn *et al*., Two physically, functionally, and developmentally distinct peritoneal macrophage subsets. *Proc. Natl. Acad. Sci. U.S.A.* **107**, 2568–2573 (2010). doi: 10.1073/pnas.0915000107; pmid: 20133793
10. A. d. A. Cassado, M. R. D'Império Lima, K. R. Bortoluci, Revisiting mouse peritoneal macrophages: Heterogeneity, development, and function. *Front. Immunol.* **6**, 225 (2015). doi: 10.3389/fimmu.2015.00225; pmid: 26042120
11. N. Zhang *et al*., Expression of factor V by resident macrophages boosts host defense in the peritoneal cavity. *J. Exp. Med.* **216**, 1291–1300 (2019). doi: 10.1084/jem.20182024; pmid: 31048328
12. J. Wang, P. Kubes, A Reservoir of Mature Cavity Macrophages that Can Rapidly Invade Visceral Organs to Affect Tissue Repair. *Cell* **165**, 668–678 (2016). doi: 10.1016/j.cell.2016.03.009; pmid: 27062926
13. S. Uderhardt, A. J. Martins, J. S. Tsang, T. Lämmermann, R. N. Germain, Resident Macrophages Cloak Tissue Microlesions to Prevent Neutrophil-Driven Inflammatory Damage. *Cell* **177**, 541–555.e17 (2019). doi: 10.1016/j.cell.2019.02.028; pmid: 30955887
14. J. F. Deniset *et al*., Gata6$^+$ Pericardial Cavity Macrophages Relocate to the Injured Heart and Prevent Cardiac Fibrosis. *Immunity* **51**, 131–140.e5 (2019). doi: 10.1016/j.immuni.2019.06.010; pmid: 31315031
15. D. S. Nelson, Reaction to antigen in vivo of the peritoneal macrophages of guinea pigs with delayed-type hypersensitivity. Effects of anticoagulants and other drugs. *Lancet* **2**, 175–176 (1963). doi: 10.1016/S0140-6736(63)92808-3; pmid: 13938029
16. J. M. Weiler, R. E. Edens, R. J. Linhardt, D. P. Kapelanski, Heparin and modified heparin inhibit complement activation in vivo. *J. Immunol.* **148**, 3210–3215 (1992). pmid: 1578145
17. J. L. Goldstein, Y. K. Ho, S. K. Basu, M. S. Brown, Binding site on macrophages that mediates uptake and degradation of acetylated low density lipoprotein, producing massive cholesterol deposition. *Proc. Natl. Acad. Sci. U.S.A.* **76**, 333–337 (1979). doi: 10.1073/pnas.76.1.333; pmid: 218198
18. M. S. Brown, S. K. Basu, J. R. Falck, Y. K. Ho, J. L. Goldstein, The scavenger cell pathway for lipoprotein degradation: Specificity of the binding site that mediates the uptake of negatively-charged LDL by macrophages. *J. Supramol. Struct.* **13**, 67–81 (1980). doi: 10.1002/jss.400130107; pmid: 6255257
19. B. Blumbach *et al*., The putative sponge aggregation receptor. Isolation and characterization of a molecule composed of scavenger receptor cysteine-rich domains and short consensus repeats. *J. Cell Sci.* **111**, 2635–2644 (1998). pmid: 9701562
20. D. M. Bowdish, S. Gordon, Conserved domains of the class A scavenger receptors: Evolution and function. *Immunol. Rev.* **227**, 19–31 (2009). doi: 10.1111/j.1600-065X.2008.00728.x; pmid: 19120472
21. N. V. L. Yap, F. J. Whelan, D. M. E. Bowdish, G. B. Golding, The Evolution of the Scavenger Receptor Cysteine-Rich Domain of the Class A Scavenger Receptors. *Front. Immunol.* **6**, 342 (2015). doi: 10.3389/fimmu.2015.00342; pmid: 26217337
22. E. Sodergren *et al*., The genome of the sea urchin *Strongylocentrotus purpuratus*. *Science* **314**, 941–952 (2006). doi: 10.1126/science.1133609; pmid: 17095691
23. U. Brykczynska *et al*., Distinct Transcriptional Responses across Tissue-Resident Macrophages to Short-Term and Long-Term Metabolic Challenge. *Cell Rep.* **30**, 1627–1643.e7 (2020). doi: 10.1016/j.celrep.2020.01.005; pmid: 32023474
24. F. S. Chia, J. Xing, Echinoderm coelomocytes. *Zool. Stud.* **35**, 231–254 (1996).
25. B. W. Hellebrekers, T. Kooistra, Pathogenesis of postoperative adhesion formation. *Br. J. Surg.* **98**, 1503–1516 (2011). doi: 10.1002/bjs.7657; pmid: 21877324
26. M. Nieuwenhuijzen, M. M. Reijnen, J. H. Kuijpers, H. van Goor, Small bowel obstruction after total or subtotal colectomy: A 10-year retrospective review. *Br. J. Surg.* **85**, 1242–1245 (1998). doi: 10.1046/j.1365-2168.1998.00841.x; pmid: 9752868
27. W. Cates, T. M. Farley, P. J. Rowe, Worldwide patterns of infertility: Is Africa different? *Lancet* **326**, 596–598 (1985). doi: 10.1016/S0140-6736(85)90594-X; pmid: 2863605
28. V. Sikirica *et al*., The inpatient burden of abdominal and gynecological adhesiolysis in the US. *BMC Surg.* **11**, 13 (2011). doi: 10.1186/1471-2482-11-13; pmid: 21658255
29. B. Kraemer *et al*., Standardised models for inducing experimental peritoneal adhesions in female rats. *BioMed Res. Int.* **2014**, 435056 (2014). doi: 10.1155/2014/435056; pmid: 24809049
30. J. M. Tsai *et al*., Surgical adhesions in mice are derived from mesothelial cells and can be targeted by antibodies against mesothelial markers. *Sci. Transl. Med.* **10**, eaan6735 (2018). doi: 10.1126/scitranslmed.aan6735; pmid: 30487249
31. S. R. Clark *et al*., Platelet TLR4 activates neutrophil extracellular traps to ensnare bacteria in septic blood. *Nat. Med.* **13**, 463–469 (2007). doi: 10.1038/nm1565; pmid: 17384648
32. C. H. Y. Wong, C. N. Jenne, B. Petri, N. L. Chrobok, P. Kubes, Nucleation of platelets with blood-borne pathogens on Kupffer cells precedes other innate immunity and contributes to bacterial clearance. *Nat. Immunol.* **14**, 785–792 (2013). doi: 10.1038/ni.2631; pmid: 23770641
33. M. Stosik, W. Deptuła, M. Trávniček, K. Baldy-Chudzik, Phagocytic and bactericidal activity of blood thrombocytes in carps (*Cyprinus carpio*). *Vet. Med.* **47**, 21–25 (2002). doi: 10.17221/5798-VETMED
34. T. Nagasawa *et al*., Phagocytosis by Thrombocytes is a Conserved Innate Immune Mechanism in Lower Vertebrates. *Front. Immunol.* **5**, 445 (2014). doi: 10.3389/fimmu.2014.00445; pmid: 25278940
35. M. B. Lawrence, T. A. Springer, Leukocytes roll on a selectin at physiologic flow rates: Distinction from and prerequisite for adhesion through integrins. *Cell* **65**, 859–873 (1991). doi: 10.1016/0092-8674(91)90393-D; pmid: 1710173
36. V. G. Martínez, S. K. Moestrup, U. Holmskov, J. Mollenhauer, F. Lozano, The conserved scavenger receptor cysteine-rich superfamily in therapy and diagnosis. *Pharmacol. Rev.* **63**, 967–1000 (2011). doi: 10.1124/pr.111.004523; pmid: 21880988
37. J. Zindel, P. Kubes, DAMPs, PAMPs, and LAMPs in Immunity and Sterile Inflammation. *Annu. Rev. Pathol.* **15**, 493–518 (2020). doi: 10.1146/annurev-pathmechdis-012419-032847; pmid: 31675482
38. L. Freyer *et al*., A loss-of-function and H2B-Venus transcriptional reporter allele for Gata6 in mice. *BMC Dev. Biol.* **15**, 38 (2015). doi: 10.1186/s12861-015-0086-5; pmid: 26498761
39. N. Faust, F. Varas, L. M. Kelly, S. Heck, T. Graf, Insertion of enhanced green fluorescent protein into the lysozyme gene creates mice with green fluorescent granulocytes and

macrophages. *Blood* **96**, 719–726 (2000). doi: 10.1182/blood.V96.2.719; pmid: 10887140
40. A. Hasenberg *et al*., Catchup: A mouse model for imaging-based tracking and modulation of neutrophil granulocytes. *Nat. Methods* **12**, 445–452 (2015). doi: 10.1038/nmeth.3322; pmid: 25775045
41. J. Zhang *et al*., CD41-YFP mice allow in vivo labeling of megakaryocytic cells and reveal a subset of platelets hyperreactive to thrombin stimulation. *Exp. Hematol.* **35**, 490–499.e1 (2007). doi: 10.1016/j.exphem.2006.11.011; pmid: 17309829
42. K. Y. Helmy *et al*., CRIg: A macrophage complement receptor required for phagocytosis of circulating pathogens. *Cell* **124**, 915–927 (2006). doi: 10.1016/j.cell.2005.12.039; pmid: 16530040
43. H. A. Schreiber *et al*., Intestinal monocytes and macrophages are required for T cell polarization in response to Citrobacter rodentium. *J. Exp. Med.* **210**, 2025–2039 (2013). doi: 10.1084/jem.20130903; pmid: 24043764
44. B. G. J. Surewaard, P. Kubes, Measurement of bacterial capture and phagosome maturation of Kupffer cells by intravital microscopy. *Methods* **128**, 12–19 (2017). doi: 10.1016/j.ymeth.2017.05.004; pmid: 28522327
45. B. McDonald *et al*., Intravascular danger signals guide neutrophils to sites of sterile inflammation. *Science* **330**, 362–366 (2010). doi: 10.1126/science.1195491; pmid: 20947763
46. E. Bianchi *et al*., Ghrelin ameliorates adhesions in a postsurgical mouse model. *J. Surg. Res.* **201**, 226–234 (2016). doi: 10.1016/j.jss.2015.10.044; pmid: 26850207
47. L. Ritsma *et al*., Surgical implantation of an abdominal imaging window for intravital microscopy. *Nat. Protoc.* **8**, 583–594 (2013). doi: 10.1038/nprot.2013.026; pmid: 23429719
48. D. Dal-Secco *et al*., A dynamic spectrum of monocytes arising from the in situ reprogramming of CCR2+ monocytes at a site of sterile injury. *J. Exp. Med.* **212**, 447–456 (2015). doi: 10.1084/jem.20141539; pmid: 25800956
49. K. D. Nolph, Z. J. Twardowski, R. P. Popovich, J. Rubin, Equilibration of peritoneal dialysis solutions during long-dwell exchanges. *J. Lab. Clin. Med.* **93**, 246–256 (1979). pmid: 429837
50. H. V. Zühlke, E. M. Lorenz, E. M. Straub, V. Savvas, Pathophysiology and classification of adhesions. [in German.] *Langenbecks Arch. Chir. Suppl. II Verh. Dtsch. Ges. Chir.* **1990**, 1009–1016 (1990). pmid: 1983476
51. A. Klingberg *et al*., Fully Automated Evaluation of Total Glomerular Number and Capillary Tuft Size in Nephritic Kidneys Using Lightsheet Microscopy. *J. Am. Soc. Nephrol.* **28**, 452–459 (2017). doi: 10.1681/ASN.2016020232; pmid: 27487796
52. C. Deppermann *et al*., Gray platelet syndrome and defective thrombo-inflammation in Nbeal2-deficient mice. *J. Clin. Invest.* **123**, 3331–3342 (2013). doi: 10.1172/JCI69210; pmid: 23863626
53. C. W. Law *et al*., RNA-seq analysis is easy as 1-2-3 with limma, Glimma and edgeR. *F1000Research* **5**, 1408 (2016). doi: 10.12688/f1000research.9005.1; pmid: 27441086
54. J. Schindelin *et al*., Fiji: An open-source platform for biological-image analysis. *Nat. Methods* **9**, 676–682 (2012). doi: 10.1038/nmeth.2019; pmid: 22743772
55. J. Y. Tinevez *et al*., TrackMate: An open and extensible platform for single-particle tracking. *Methods* **115**, 80–90 (2017). doi: 10.1016/j.ymeth.2016.09.016; pmid: 27713081
56. J. Zindel, M. Peiseler, M. Hossain, C. Deppermann, W. Y. Lee, B. Haenni, B. Surewaard, D. Candinas, P. Kubes, Primordial GATA6 macrophages function as extravascular platelets in sterile injury, Dryad (2021). doi: 10.5061/dryad.05qfttf1w

ACKNOWLEDGMENTS

We thank T. Nussbaumer for the breeding of mice, K. Poon at the Nicole Perkins Microbial Communities Core Lab for assistance with flow cytometry, A. K. Chojnacki at the Live Cell Imaging Resource Laboratory for assistance with Imaris software, R. Sidhu from Leica Microsystems for technical assistance, and P. Furer for manufacturing abdominal imaging windows. Electron microscopy sample preparation and imaging were performed with devices supported by the Microscopy Imaging Center (MIC) of the University of Bern. **Funding:** J.Z is supported by a fellowship from the Swiss National Science Foundation (SNSF P1BEP3_181164). C.D. and M.P. are supported by Deutsche Forschungsgemeinschaft (DFG) Research Fellowships (DE 2654/1-1 and PE 2737/1-1, respectively). M.H. is supported by a Banting Fellowship. J.F.D. and B.G.J.S. are supported by a fellowship from Canadian Institutes of Health Research. P.K. is supported by the NSERC Discover grant (RGPIN/07191-2019), the Heart and Stroke Foundation of Canada, Canadian Institutes of Health Research, and the Canada Research Chairs Program.
Author contributions: J.Z. designed the experiments and developed the peritoneal pouch model. J.Z. and P.K. wrote the manuscript, with input from all authors. M.P., M.H., W.Y.L., B.G.J.S., and D.C. helped design and execute experiments. J.F.D. provided RNA-seq data of cavity macrophages and helped with the analysis and interpretation of RNA-seq data. C.D. provided expertise and help with platelet isolation and aggregometry. B.H. and B.Z. provided expertise and help with electron microscopy experiments.
Competing interests: The authors declare no competing interests.
Data and materials availability: Expression datasets used are available at Gene Expression Omnibus (GSE131724 and GSE133127). Raw data for this article are deposited at Dryad (*56*). All other data are available in the main text or the supplementary materials.

SUPPLEMENTARY MATERIAL

science.sciencemag.org/content/371/6533/eabe0595/suppl/DC1
Figs. S1 to S8
Tables S1 and S2
MDAR Reproducibility Checklist
Movies S1 to S6

View/request a protocol for this paper from *Bio-protocol*.

29 July 2020; accepted 8 January 2021
10.1126/science.abe0595

Primordial GATA6 macrophages function as extravascular platelets in sterile injury

J. ZindelM. PeiselerM. HossainC. DeppermannW. Y. LeeB. HaenniB. ZuberJ. F. DenisetB. G. J. SurewaardD. CandinasP. Kubes

Science, 371 (6533), eabe0595.

Macrophages seal 'em in the coelom

GATA6 macrophages resident in body cavities exhibit both phagocytic and repair functions. However, the mechanisms by which these cells can identify and migrate to sites of injury have remained unclear. Using intravital imaging of mouse peritoneal cavities, Zindel *et al.* report that GATA6 macrophages rapidly assemble clot-like structures in a process strongly analogous to thrombosis (see the Perspective by Herrick and Allen). The formation of these aggregates requires the expression of macrophage scavenger receptor domains and acts to plug wounds and promote healing. This pathway can be inadvertently activated during medical procedures, when macrophage aggregates can promote the generation of abdominal scar tissue known as adhesions. Inhibition of macrophage scavenger receptors may therefore be a useful therapeutic approach after surgeries that cause injury to body cavities.

Science, this issue p. eabe0595; see also p. 993

Science (ISSN 1095-9203) is published by the American Association for the Advancement of Science. 1200 New York Avenue NW, Washington, DC 20005. The title *Science* is a registered trademark of AAAS.